# Influence of NH$_4$Cl additive in a VO$^{2+}$/VO$_2^+$ - AQDS/AQDS$^{2-}$ solar redox flow battery

Gengyu Tian [a], Rhodri Jervis [b,c], Ana Jorge Sobrido [a,c,*]

[a] School of Engineering and Materials Science, Queen Mary University of London, London E1 4NS, United Kingdom
[b] Electrochemical Innovation Lab, Department of Chemical Engineering, University College London, WC1E 7JE, United Kingdom
[c] The Faraday Institution, Quad One, Harwell Science and Innovation Campus, United Kingdom of Great Britain and Northern Ireland, Didcot OX11 0RA, United Kingdom

ARTICLE INFO

ABSTRACT

Solar redox flow batteries are a relatively new type of redox flow battery technology that uses solar energy to directly store chemical energy. Here we present a solar redox flow battery that uses a MoS$_2$@TiO$_2$ thin film with a Nafion protection layer supported on FTO glass substrate as photoanode, employing VO$^{2+}$/VO$_2^+$ and AQDS/AQDS$^{2-}$ as redox active species. When the solar radiation strikes the photoelectrode, the photogenerated holes oxidize VO$^{2+}$ to VO$_2^+$, while the photogenerated electrons reduce AQDS to AQDS$^{2-}$ at the counter electrode. The oxidized form of V$^{5+}$ and reduced form of AQDS$^{2-}$ thus retain the chemical energy and can release the stored charged *via* the reverse electrochemical reaction. The addition of NH$_4$Cl to the electrolyte was found to have a positive impact on the electrochemical performance of the redox flow cell. This effect was more evident for the VOSO$_4$ electrolyte, leading to an enhancement of the voltaic and energy efficiencies of more than 17.5%. The results suggest that NH$_4$Cl promotes both mass transport of the vanadium redox species and charge transfer of the AQDS in the electrolyte. The solar-to-output energy conversion efficiency (SOEE) of the solar redox flow battery using 1.6 g L$^{-1}$ NH$_4$Cl in both anolyte and catholyte reached 9.73%, and an energy density of 87.45% after 10 consecutive one-hour photocharging cycles. Additionally, the use of Nafion to protect the MoS$_2$@TiO$_2$ photoanode from photocorrosion was explored. The Nafion layer ensured an increased stability of MoS$_2$@TiO$_2$ against the strong acidic environment while maintaining effective light response, which translated into enhanced photon and mass transport. An energy storage capacity of ~60 mAh L$^{-1}$ after 1-hour photocharging was observed.

## 1. Introduction

The demand for renewable clean energy in the global market has grown rapidly due to the imminent energy crisis. Taking the 2020 report released by the US Energy Information Administration (EIA) as reference, solar and wind energy technologies account for more than half of the entire renewable energy harvesting market. According to this report, the total renewable energy reached 792 billion kWh, 19.8% of the total power generation in the United States, of which wind power accounted for 8.4% and hydropower for 7.3%, while solar energy accounted for 2.3%.

Due to the discontinuous nature of solar and wind resources, the harvested energy cannot be directly integrated into the grid as electrical energy. Therefore, the utilization of this type of renewable energy places high demands on large-scale energy storage and grid balancing systems.

Redox flow batteries have made significant progress in recent years as contender for grid-scale electrochemical energy storage and have attracted considerable attention [1–5], due to their potential low cost, relative simplicity in operation and materials, and scalability in energy capacity. Most commercialized redox flow batteries use vanadium as the redox species, but due to the high cost of vanadium and its harmfulness to the environment, alternative chemistries have been investigated [6, 7]. Among them, organic redox couples have been widely developed in the last few years, due to their design flexibility [8–10]. For example, quinones possess favourable chemical and electrochemical properties that enable a wide range of reduction potentials and solubility, by adding specific functional groups [11–13]. Of these, AQDS (9, 10-anthraquinone-2,7-disulphonic acid) has an extremely rapid and reversible two-electron, two-proton electrochemical process on a glassy carbon electrode in acid [14]. In addition, anthraquinone species can be

---

synthesized from inexpensive commodity chemicals [15].

The use of electrolyte additives has been demonstrated to be successful in enhancing the ionic conductivity of the electrolyte [16–18]. The increase in ion mobility in the electrolyte can enhance the redox kinetics, thereby reducing the overpotential in practical cycling, enabling the battery to achieve higher capacity [19]. One example is ammonium chloride ($NH_4Cl$) which has been studied as additive for vanadium electrolyte and shows double the capacity compared to additive-free electrolytes after 100 cycles, and an absolute capacity of 0.45 Ah [20]. An outstanding enhancement of 25% of battery capacity was achieved in a zinc-iodine redox flow battery after addition of $NH_4Cl$, which enhanced solubility of iodine [21] and AQDS [22]. In addition, by promoting the vanadium dispersion capability, $NH_4Cl$ also prevents precipitation issues [20]. The hydrolysis reaction of $NH_4^+$ boosts the conductivity of the electrolyte [23], but also acts as buffer, avoiding unwanted pH change of the electrolyte that could decrease the activity of the pH-sensitive reaction during the functioning of the battery [24]. The redox potential of many organic redox species, such as phenazine/alloxazine and quinones are affected by the pH of the electrolyte and thus the cell potential [25,26]. Solar redox flow batteries (SRFB), able to directly collect and store solar energy, are attracting increasing interest [27–29]. However, the technology is still in its infancy and many aspects need to be optimized to become competitive. One of the components that requires attention is the photoelectrode. The main strategies to increase stability and efficiency of the photoelectrode involve the use of heterojunctions or surface functionalization [30–33]. Here we have developed a photoelectrode based on $TiO_2$, a semiconductor widely employed in photoelectrochemical cells [34–36] and more recently in SRFBs [37–39], decorated with molybdenum disulfide ($MoS_2$), component that extends the photoelectrode light absorption into the visible [40,41] and recently demonstrated as photoelectrode in a SRFB [42]. To overcome stability problems previously detected [42], the $MoS_2@TiO_2$ photoelectrode was protected with a layer of Nafion® which successfully increased the stability under acidic conditions. The redox system studied was $VO^{2+}/VO_2^+$ as anolyte and $AQDS/AQDS^{2-}$ as catholyte and the effect of $NH_4Cl$ electrolyte additive for both redox couples was investigated. Fig. 1 shows the schematic view of the SRFB using Nafion-protected $MoS_2@TiO_2$ as the photoelectrode with $NH_4Cl$ as additive. In the anolyte, the $VO^{2+}$ will oxidize to $VO_2^+$ in the solar redox cell in the photocharging process and reduce from $VO_2^+$ back to $VO^{2+}$ in the redox cell. The opposite process will happen to AQDS in the catholyte. Nafion-protected $MoS_2@TiO_2$ exhibited a photocurrent density of 0.5 mA cm$^{-2}$, 20% higher than bare $MoS_2@TiO_2$. The energy efficiency of the redox flow battery increased by 22.5% after the addition of $NH_4Cl$. Nafion-protected photocharging energy density reached a value of 48.63 Wh L$^{-1}$ after 1-hour photocharging, with a remaining energy density after 10 photocharge / discharge cycles of 87.45%.

## 2. Experimental

### 2.1. Electrochemical characterization

A three-electrode electrochemical cell was employed to study the electrochemical behavior of the carbon felt electrode against the vanadium and the AQDS redox species, separately. The carbon felts (3.18 mm thick, 99.0%, Alfa Aesar) were pre-treated in a tubular furnace (TS1–1200, CARBOLITE GERO) at 800 °C for 2 h, using a heating rate of 3.0 °C min$^{-1}$ and a nitrogen flow rate of 0.5 L min$^{-1}$ [43]. A 1.0 cm$^2$ (0.318 cm$^3$) carbon felt electrode, held by a PTFE supported platinum film, acted as the working electrode, and KCl saturated calomel $Hg_2Cl_2$ electrode (SCE) and Pt foil were employed as the reference and counter electrodes, respectively. Cyclic voltammetry (CV) experiments were conducted between -0.5 V to 0.5 V and 0.1 V to 1.4 V *versus* SCE, at a scan rate of 10, 20, 30, 40, and 50 mV s$^{-1}$, and electrolyte with a concentration of 0.1 M $VOSO_4$ (vanadium IV oxide sulfate hydrate, Sigma-Aldrich, 97%) and 0.05 M AQDS (2,7-disulfonic acid disodium



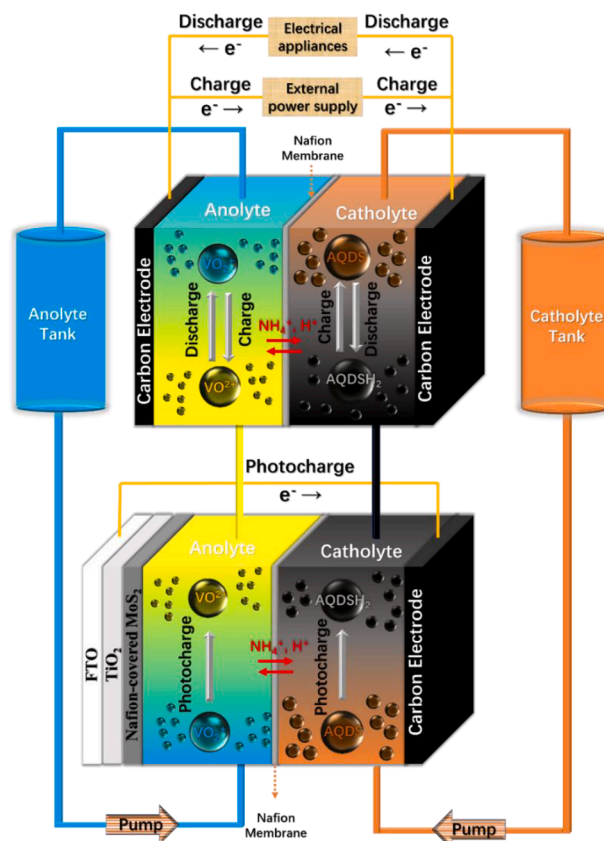**Fig. 1.** Schematic view of the SRFB studied in this work: C (s)| $VO^{2+}$, $VO_2^+$|| AQDS, $AQDS^{2-}$|C (s) redox flow battery, and Nafion-protected $MoS_2$(s)/TiO2| $VO^{2+}$, $VO_2^+$||AQDS, $AQDS^{2-}$|C (s).

salt, Santa Cruz) with 3.0 M $H_2SO_4$ (Sigma, 98%) and $NH_4Cl$ (Ammonium chloride, Sigma-Aldrich). Electrochemical impedance spectroscopy (EIS) experiments were conducted using a frequency range of 0.1 MHz to 0.1 Hz and a perturbation of 10.0 mV.

RFB testing was performed in a cell consisting of two graphite plates with a 5.0 cm$^2$ interdigitated flow field. The channel width, depth and length were 0.2, 0.2 and 2.2 mm, respectively. Two pre-treated carbon felts (not pressed) were placed on each graphite plate, sealed by two Teflon gaskets with 40 mm diameter "O" Rings (nitrile 70) facing the Nafion® membrane. Two gold-plated copper plates serve as current collectors. The flow cell was assembled using two stainless-steel endplates tightened with eight bolts and compression by torque wrench (1.2 N m).

Nafion membranes were treated before use as follows: first, soaked in 50 mL of 5 wt.% $H_2O_2$ 80 °C for 1 h, then in 80 °C distilled water for 1 h, and then in 80 °C for an additional 1 h in 3.0 M $H_2SO_4$. The membrane was finally treated at 80 °C for 1 h in distilled water. A volume of 20 mL was employed as initial catholyte and anolyte, respectively. The electrolyte was pumped using a peristaltic pump with double head, and flow rate on both anolyte and catholyte of 2.5 mL min$^{-1}$. The size of carbon felt as working electrode for redox flow battery testing was 5.0 cm$^2$ (1.59 cm$^3$).

Charge-discharge experiments were conducted in the voltage range 0.2 to 1.6 V at current densities of 4.0 mA cm$^{-2}$, 10.0 mA cm$^{-2}$, and 20.0 mA cm$^{-2}$, and 0 to 1.2 V at a current density of 10.0 mA cm$^{-2}$ with 0.1 M $VOSO_4$ as anolyte and 0.05 M AQDS as catholyte, and different concentration of $NH_4Cl$. The electrolyte was pre-discharged to 0 V at a current density of 0.1 mA cm$^{-2}$. Pre-treated carbon felts separated by a Nafion® membrane (115, 0.0127 cm. thick, DuPont de Nemours & Co) were used as positive and negative electrodes. The discharge current density after photocharging was 0.4 mA cm$^{-2}$.

## 2.2. Photoelectrode synthesis and photoelectrochemical characterization

TiO$_2$ nanorod arrays (NRs) on FTO were prepared using a hydrothermal method [44]. Briefly, 60 mL of deionized water was mixed with 30 mL of concentrated hydrochloric acid (36.5% by weight) and the solution was sonicated for 15 min. Then, 0.5 mL of titanium (IV) butoxide (purity, ≥97%, gravimetric, Sigma) was added to the solution and sonicated for an additional 15 min. The FTO substrate was placed into a Teflon liner (200 mL) whereupon the hydrothermal synthesis was carried out at 180 °C for 12 h. The resulting samples were rinsed thoroughly with deionized water, then dried at 80 °C for 1 hour and heat treated in air at 500 °C for 1 h.

MoS$_2$ nanoflowers were grown onto the TiO$_2$ NRs by a facile hydrothermal reaction [27]. Firstly, 242 mg (0.001 mol) Na$_2$MoO$_4$·2H$_2$O powder (99%, Sigma) and 242 mg (0.002 mol) L-Cysteine (99.99%, Sigma) were mixed in 90 mL deionized water with magnetic stirring for 10 min, then transferred to a liner (Teflon). Subsequently, the TiO$_2$ NRs were placed into the liner containing the MoS$_2$ precursors and put the liner into the autoclave. The hydrothermal synthesis and deposition of MoS$_2$ onto the TiO$_2$ NRs were conducted at 200 °C for 12 h, followed by rinsing with deionized water and drying at 80 °C for 1 h. The resultant samples were labelled as MoS$_2$@TiO$_2$. A drop of Nafion (5%, 0.1 mL cm$^{-2}$) was drop-cast on the surface of MoS$_2$@TiO$_2$ and labelled as Nafion-protected MoS$_2$@TiO$_2$.

The SRFB consisted of a modified redox flow cell, with a window in the anolyte side to enable the irradiation from the light source to reach to the photoanode. The solar cell connected with the redox flow cell, two electrolyte tanks and a double-head peristaltic pump (Watson-Marlow 030.3134.3DU) by PTFE tubing. The solar flow cell assembly included the photoelectrode and carbon felt, separated by a Nafion® 115 membrane. Both carbon felts and Nafion® membranes were pre-treated as described in the previous section. Photocharging of the SRFB was conducted without any external bias through irradiation of the photoanode using simulated solar light (450 W Xe lamp) using an AM 1.5 G filter. 5.0 cm$^2$ is the illuminated area of the photoelectrode in the solar flow cell. All the electrochemical experiments were carried out using a potentiostat (Gamry IFC5000–05,520).

## 3. Result and discussion

### 3.1. Three-electrode system

To understand the electrochemical performance of the VOSO$_4$ and AQDS redox pairs independently with NH$_4$Cl additive, cyclic voltammetry experiments were conducted. AQDS exhibited stable electrochemical performance at different NH$_4$Cl concentrations, while VOSO$_4$ showed enhanced side reactions: oxygen evolution reaction (OER) and chlorine evolution reaction (CER) in the voltage range above 1.36 V vs SHE (Fig. 2). VOSO$_4$ presents oxidation and reduction peaks around 1.23 V and 0.53 V (vs SCE), respectively while AQDS shows oxidation and reduction peaks around 0.22 V and −0.22 V (vs SCE), respectively. The average redox center of 5 different NH$_4$Cl concentration in VOSO$_4$ and AQDS is 0.88 V and −0.018 V vs SCE, separately. The redox reaction of VOSO$_4$ and AQDS can be presented as follows (the structural formula of the AQDS during reaction can be seen in the supporting information, Equation S1):

$$AQDS + 2e^- + 2H^+ \rightleftharpoons AQDSH_2 \qquad (1)$$

$$VO^{2+} \rightleftharpoons VO_2^+ + e^- \qquad (2)$$

With increasing scan rate, VOSO$_4$ (Fig. 3a) and AQDS (Fig. 3b) oxidation and reduction peak widths and separation increase. Figs. 3c and 3d show the dependence of the position of the redox peaks with the scan rate for VOSO$_4$ and AQDS, respectively. The increase of the oxidation and reduction peak currents density versus square root of scanning rates fits a linear relationship and can be used to estimate the
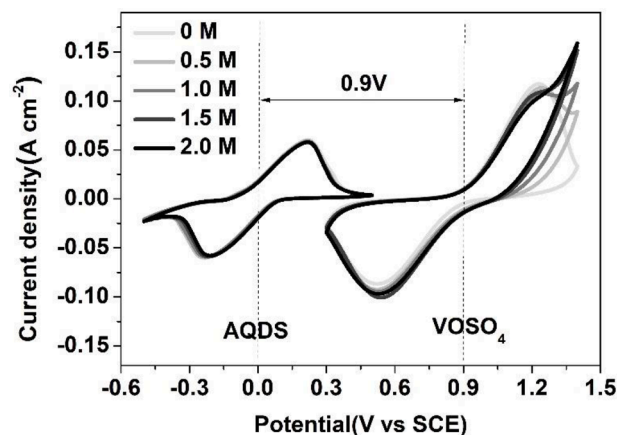


**Fig. 2.** CV of four different NH$_4$Cl concentration (0.5, 1.0, 1.5 and 2.0 M) in 0.1 M AQDS or VOSO$_4$ with 3.0 M H$_2$SO$_4$ at scan rate of 10 mv $s^{-1}$.

diffusion coefficient of the redox ion.

The electrochemical activity of NH$_4$Cl in VOSO$_4$ and AQDS (Figure S1) was studied using CV at different scan rates in four NH$_4$Cl concentrations (0.5, 1.0, 1.5 and 2.0 M). The oxidization peak corresponding to AQDS could be detected at low scan rate. The increase in NH$_4$Cl concentration promoted the chlorine evolution reaction. However, at higher scan rate, the effect of NH$_4$Cl becomes less obvious. In the case of the VO$^{2+}$ / VO$_2^+$, on the contrary, the current density peak decreases with increasing NH$_4$Cl concentration. In the meantime, the potential gap between oxidation and reduction processes increases, suggesting that only a specific concentration of NH$_4$Cl can effectively promote redox activity.

Because both VOSO$_4$ and AQDS behave differently versus NH$_4$Cl, a comparison between different NH$_4$Cl concentration should be conducted. EIS experiments were carried out to study further the effect of NH$_4$Cl (Fig. 4a and b) The equivalent circuit to simulate and fit the EIS data is shown in Fig. 4(c) for the VOSO$_4$ and Fig. 4(d) for the AQDS. R1 represents the system resistance, which includes the resistance of the electrolyte and ion transport through the membrane, as well as the electrical resistance of the cable connection. In this case, R2 and CPE1 represent the electrode-electrolyte interface double layer between carbon felt and electrolyte, showing the electron-transfer of VOSO$_4$ or the first electron-transfer of AQDS. R3 and CPE2 represent the second electrode-electrolyte double layer between carbon felt and electrolyte, indicating the second electron-transfer of AQDS. These two double layers describe the charge transfer process of AQDS. The Warburg element (W) series after illustrates the diffusion process (mass transfer process). The relevant parameters can be extracted by the fitting model shown in Table S1 and S2, Support Information. The EIS simulation results are consistent with the diffusion coefficients estimated using CV. Even though the highest diffusion coefficient of VOSO$_4$ is reached at 1.0 M NH$_4$Cl, calculated from the CV, the NH$_4$Cl influence in the increase of side reactions (especially hydrogen evolution reaction) causes the deviation of the oxidation peak position, and therefore the EIS analysis represents a more accurate method to study the diffusion of VOSO$_4$ at different NH$_4$Cl concentrations.

Fig. 3(a) shows that the fastest mass transport and charge transfer at the electrolyte / electrode interface for VOSO$_4$ are obtained at 1.5 M NH$_4$Cl. The fitting results (Table S1) show that the addition of increasing amounts of NH$_4$Cl to the electrolyte leads to an expected decrease of the solution resistance (R1), reaching its lowest point at 1.5 M NH$_4$Cl. Moreover, both charge transfer resistance (R2) reach minimum values at 1.5 M NH$_4$Cl. Meanwhile the mass transfer resistance (W) keeps increasing as NH$_4$Cl concentration increasing. CPE1-T and CPE1-P fitting results show that as NH$_4$Cl concentration increases, the double layer exhibits more a capacitor-like with higher capacitance.
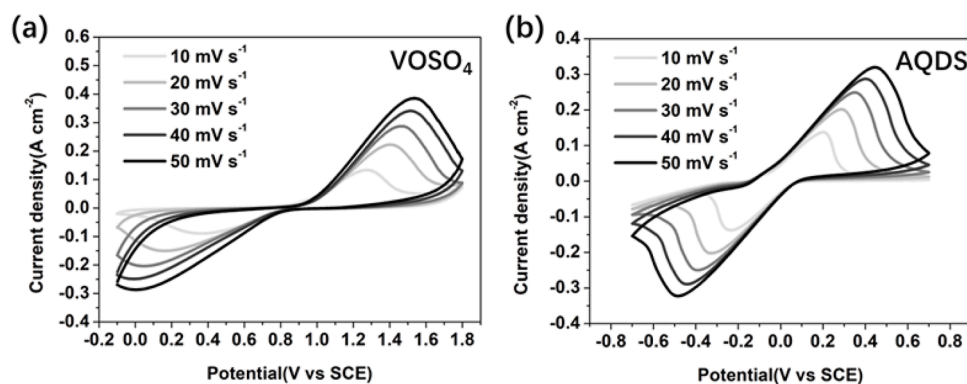
**Fig. 3.** CVs of (a)0.1 M VOSO$_4$ and (b)0.05 M AQDS at different scan rates.



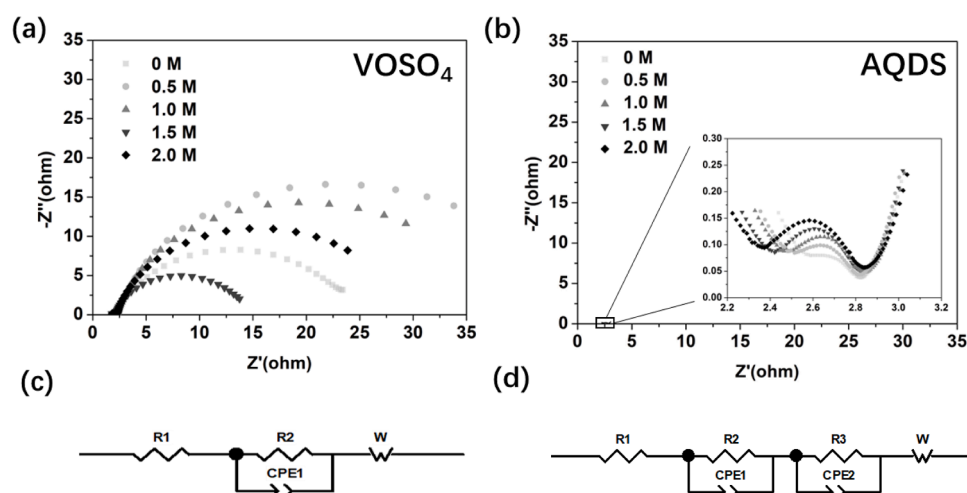**Fig. 4.** EIS data of (a)0.1 M VOSO$_4$ and (b)0.05 M AQDS and their (c, d) equivalent circuit for the EIS simulation in 0 M, 0.5 M, 1.0 M, 1.5 M, and 2.0 M NH$_4$Cl with 3.0 M H$_2$SO$_4$.

The addition of NH$_4$Cl did not have an obvious impact on the resistance of the electrolyte (R1) for the AQDS (Table S2). As the concentration of NH$_4$Cl increased, R2 decreased while R3 increased, but the total changes were not significant. A contrary trend is observed with the CPE1-P and CPE2-P of AQDS, which exhibit a more capacitor-like behavior and lower capacitance accumulation (CPE1-T+ CPE2-T) when increasing NH$_4$Cl concentration. The formation of a NH$_4^+$ - AQDS bond may allow electrons to move more easily, thereby decreasing the interface transfer resistance. Even though the change is small, the fitting results of AQDS indicate that increasing the NH$_4$Cl concentration will cause the W-R to decrease, which is consistent with

the diffusion coefficient estimated by CVs.

To study the solution resistance in isolation from the redox behaviour of the active materials, three-electrode EIS tests were conducted, and the result is presented in Figure S2(a). It is obvious NH$_4$Cl does not have much effect on the solution resistance, but there is a clear trend that shows the higher the NH$_4$Cl concentration, the faster the mass transfer rate.

### 3.2. Redox flow battery

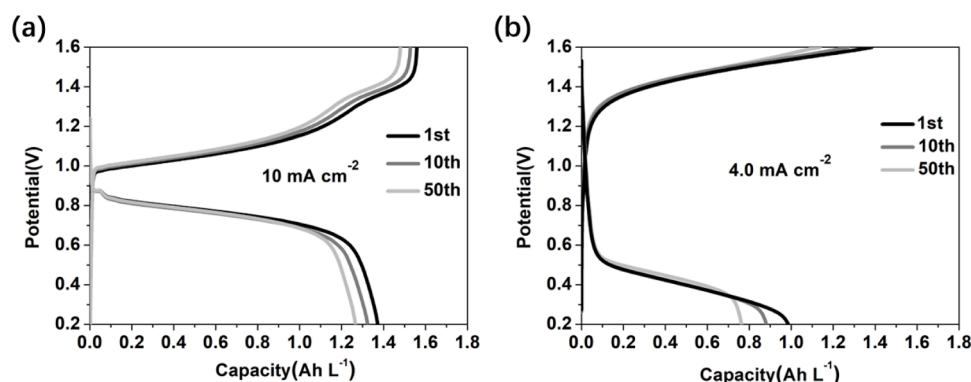Fig. 5 shows the charge-discharge curves for a redox flow battery



**Fig. 5.** Cyclic charge-discharge (0.2 V-1.6 V) of 0.1 M VOSO$_4$ and 0.05 M AQDS with 3.0 M H$_2$SO$_4$ under (a) 10.0 mA cm$^{-2}$, and (b) 20.0 mA cm$^{-2}$.

using VOSO$_4$ as anolyte and AQDS as catholyte, without addition of NH$_4$Cl, at different current densities. The current applied to the RFB in this work is very low compared to a typical RFB. This is because the charging photocurrent in a SRFB is lower than in a RFB, so for a better comparison, it is investigated how the RFB can charge and discharge current values of the same order of magnitude than a SRFB [29,45]. A smaller current density (Fig. 5a, 10.0 mA cm$^{-2}$) results in lower electrochemical polarization. On the contrary, a higher current density (20 mA cm$^{-2}$) will reduce the reversibility of the redox reaction. To make

the system energy utilization more efficient, the current density of 10.0 mA cm$^{-2}$ was selected for both charge and discharge experiments.

To investigate to what extent NH$_4$Cl can mitigate some of the side reactions at deep state of charge, the charge-discharge test potential range was changed from 0.2–1.6 V to 0–1.2 V to ensure the battery was fully discharged and reduce the side reactions caused by overcharging.

The addition of NH$_4$Cl enhances the performance of the battery, not only in terms of capacity loss per cycle, but also voltage efficiency (Fig. 6 and Table 1). The addition of NH$_4$Cl is expected to also increase the
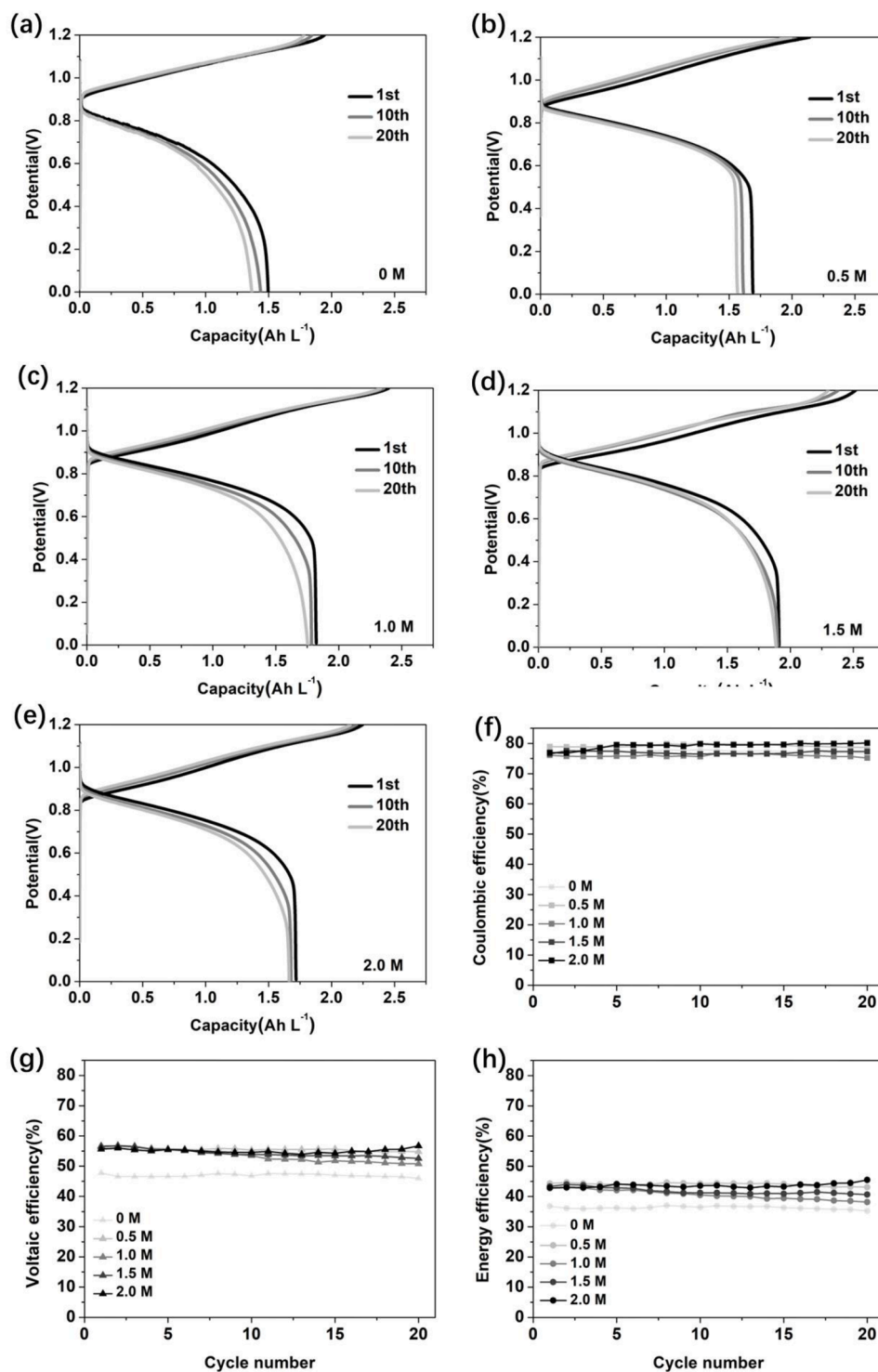


**Fig. 6.** Cyclic Charge-Discharge of (a) 0 M, (b) 0.5 M, (c) 1.0 M, (d) 1.5 M, and (e) 2.0 M NH$_4$Cl under 10.0 mA cm$^{-2}$ in 0.1 M VOSO$_4$ and 0.05 M AQDS with 3.0 M H$_2$SO$_4$. (f) Coulombic efficiency (CE), (g) Voltaic efficiency (VE) and (h) Energy efficiency (EE) of the series cyclic charge-discharge.

**Table 1**
Average charge-discharge capacity and capacity loss.

| $NH_4Cl$ concentration | Average charge capacity (Ah L$^{-1}$) | Average discharge capacity (Ah L$^{-1}$) | Storage capacity loss per cycle |
|---|---|---|---|
| 0 M | 1.85 | 1.44 | 0.67% |
| 0.5 M | 2.05 | 1.62 | 0.6% |
| 1.0 M | 2.36 | 1.78 | 0.35% |
| 1.5 M | 2.34 | 1.90 | 0.1% |
| 2.0 M | 2.20 | 1.69 | 0.17% |

thermal stability based on previous observations VRFB [46]. Due to steric hindrance and coulomb repulsion, $VO_2^+$ ions exhibit poor thermal stability and are prone to $V_2O_5$ precipitation above 40 °C, which seriously affects the working life of VRFBs. After adding $NH_4Cl$, the precipitation problem of $VO_2^+$ ions can be relieved, because the ammonium group is easily adsorbed on the $VO_2^+$ ions, which enhances the dispersion ability of the $VO_2^+$ ions, hinders its crystal growth, and improves its thermal stability in the high-temperature range. In addition, chloride ions contained in $NH_4Cl$ can enhance its thermal stability by forming a mixture with sulfate ions in $VOSO_4$ [47]. Additionally, it has been reported that the differences in VE and EE are caused by the fact that $NH_4Cl$ prevents the precipitation or hydrolysis of $VO_2^+$ ions and reduces the overpotential of the RFB [20].

The average practical charging and discharging capacity of 1.5 M $NH_4Cl$ in RFB was 2.34 Ah L$^{-1}$ and 1.90 Ah L$^{-1}$, respectively. During the 1st cycle in 1.5 M $NH_4Cl$, the charge capacity reaches 2.52 Ah L$^{-1}$ and remains 2.30 Ah L$^{-1}$ after 20 cycles. The discharge capacity remains 1.89 Ah L$^{-1}$ at the 20th cycle with 1.91 Ah L$^{-1}$ discharge capacity at the 1st cycle. When the $NH_4Cl$ concentration is 1.0 M, the average charged capacity reached highest value of 2.36 Ah L$^{-1}$, but the discharge capacity is relatively low compared to 1.5 M $NH_4Cl$. Indeed, the minimum value of capacity loss for RFB took place at 1.5 M $NH_4Cl$. With respect to the diffusion coefficient, while vanadium exhibited the fastest diffusion rate in 1.0 M $NH_4Cl$, which resulted in the highest charging capacity measured, the diffusion rate of ADQS in 1.0 M $NH_4Cl$ was much lower. A concentration of 1.5 M $NH_4Cl$ was found to be a good compromise for both redox species.

A possible reason for the capacity loss is the crossover effect typically observed in VRFBs [48]. The crossover process is a combination of osmotic and electroosmotic processes that cause battery self-discharge [49]. This process is complicated; not only the transfer coefficient of the ion-exchange membrane in the electrolyte, but also the concentration and diffusion speed of ions in the electrolyte under different bias voltages need to be considered [24].

$NH_4^+$ and $H^+$ are the main charge carriers passing through the Nafion membrane. Since the ionic strengths on both sides are similar, the osmotic pressure is relatively small. The volume between the two sides did not change significantly during the long-term experiments.

Coulombic efficiency (CE), voltaic efficiency (VE) and energy efficiency (EE) can be determined according to the following equations [50], respectively, and they were calculated and plotted as Fig. 6(f)–(h).

$$CE = \frac{\int I_d dt}{\int I_c dt} \times 100\% = \frac{\sum_0^{m-1} \frac{1}{2}\left(I_j + I_{j+1}\right)\left(t_{j+1} - t_j\right)}{\sum_0^{n-1} \frac{1}{2}(I_k + I_{k+1})(t_{k+1} - t_k)} \times 100\%$$

$$VE = \frac{\sum_0^{m-1} \frac{1}{2}\left(V_j + V_{j+1}\right)\left(t_{j+1} - t_j\right)}{\sum_0^{n-1} \frac{1}{2}(V_k + V_{k+1})(t_{k+1} - t_k)} \times 100\%$$

$$EE = CE \times VE = \frac{\int V_d I_d dt}{\int V_C I_C dt} \times 100\%$$

where $I_c$, $V_c$, $I_k$, $V_k$, $t_k$ denote current, voltage and reaction time during the charge, while $I_d$, $V_d$, $I_j$, $V_j$, $t_j$ denote current, voltage and reaction time during the discharge, respectively.

The average coulombic efficiency before and after the addition of

$NH_4Cl$ does not vary significantly. However, $NH_4Cl$ can significantly enhance the performance, resulting in improved energy efficiency. The reason behind this phenomenon may be that $NH_4^+$ can not only effectively improve the conductivity of the electrolyte, prevents the precipitation or hydrolysis of $VO_2^+$ ions and reduces the overpotential of RFB, but also help the electrodes achieve faster charge balance through the membrane [24,45]. Though the improvement of VE and EE is obvious, the value of them is comparably low due to the crossover of vanadium ions and AQDS. Additionally, the low redox species concentration also contributed to the low efficiency. This is not only because the resistance of charge transfer increases as the concentration of redox species decreases, but also because of a concentration overpotential - there is not enough reactant species available when in low concentration or towards the end of charge or discharge [51]. The relatively low flow rates also have an effect on VE and EE: the concentration overpotential decreases as the flow rate decreases [52].

### 3.3. Solar redox flow battery

For the testing in a SRFB set up, the negative electrode carbon felt was replaced by a photoelectrode ($MoS_2$@$TiO_2$). The photoelectrode developed in this work is a modification of a previously reported one [42]. In this case, a protective layer of Nafion has been added to the top of the $MoS_2$@$TiO_2$. Since Nafion possesses negatively charged hydrophilic sulfonate groups [53,54], it can repel negatively charged ions like $SO_4^{2-}$, preventing $MoS_2$ from reacting with it, but also attracts positively charged ions, accelerating the transfer process of $VO^{2+}$ to $VO_2^+$, making the photoelectrode more efficient. The SEM images of $TiO_2$, $MoS_2$@-$TiO_2$, and Nafion-protected $MoS_2$@$TiO_2$ are shown in Fig. 7. The thickness of the $TiO_2$ nanoarrays, $MoS_2$ nanoflowers, and Nafion protective layers are 2.83, 0.75, 2.25 μm, respectively (Fig. 7(e)).

UV–Vis results (Figure S2(b)) show that with the help of $MoS_2$, the photoanode can absorb more light energy than when only $TiO_2$ is used, and, after being covered by Nafion, the photoanode can collect more light energy. However, the absorbance intensity does not change much compared to before the coverage. The photoanode contacts the anolyte directly, so stability is a vital parameter for the photoanode to endure the corrosion due to the strong acidic conditions. The stability of the $MoS_2$@$TiO_2$ photoelectrode published in our last paper is not good and the photocurrent density has an obvious loss in 5 cyclic photocharge. In this work, this problem has been fully solved by covering Nafion on the top of the $MoS_2$@$TiO_2$ photoanode. The photoelectrode can work stably in 10 h under light without obvious photocurrent density loss.

FTIR results are shown in Figure S2(c). For the Nafion- protected $MoS_2$@$TiO_2$, the spectral envelope around 1212 cm$^{-1}$ is mainly composed of -$CF_2$ symmetric and asymmetric stretch bands, -$CF_3$ asymmetric stretch bands, and -$SO_3$- asymmetric stretch bands [55]. A typical absorption band at 1558 cm$^{-1}$ was assigned to H—O-H bending vibration [56]. After Nafion coverage, the signal strength of Nafion-protected $MoS_2$@$TiO_2$ dropped significantly. The characteristic peaks are identical to those of Nafion-protected $MoS_2$@$TiO_2$ [57]. In addition, XPS results in Figure S2(d) confirmed the presence of the Nafion layer covering the surface of $MoS_2$@$TiO_2$.

In the case of the SRFB, 1.5 M $NH_4Cl$ was also added to both catholyte and anolyte. Although the photocurrent density increased slightly when the $NH_4Cl$ concentrations were at 1.5 M in the first 10 min, the rest of the illumination time (50 min) showed that the $NH_4Cl$ concentration did not have a significant effect on the photoelectrode performance. This phenomenon suggests that with a more efficient photoelectrode, the photocurrent enhancement due to $NH_4Cl$ should be more pronounced. Compared to the bare $MoS_2$@$TiO_2$, the photocurrent density of the Nafion-protected $MoS_2$@$TiO_2$ was increased by near 20% (Fig. 8a). The system exhibited good resistance to photocorrosion after 10 h of 1h-photocharging cycles [42]. This demonstrated that the Nafion layer is capable of effectively protecting the $MoS_2$@$TiO_2$, while also contributing to charge carrier separation and transport, as suggested by the
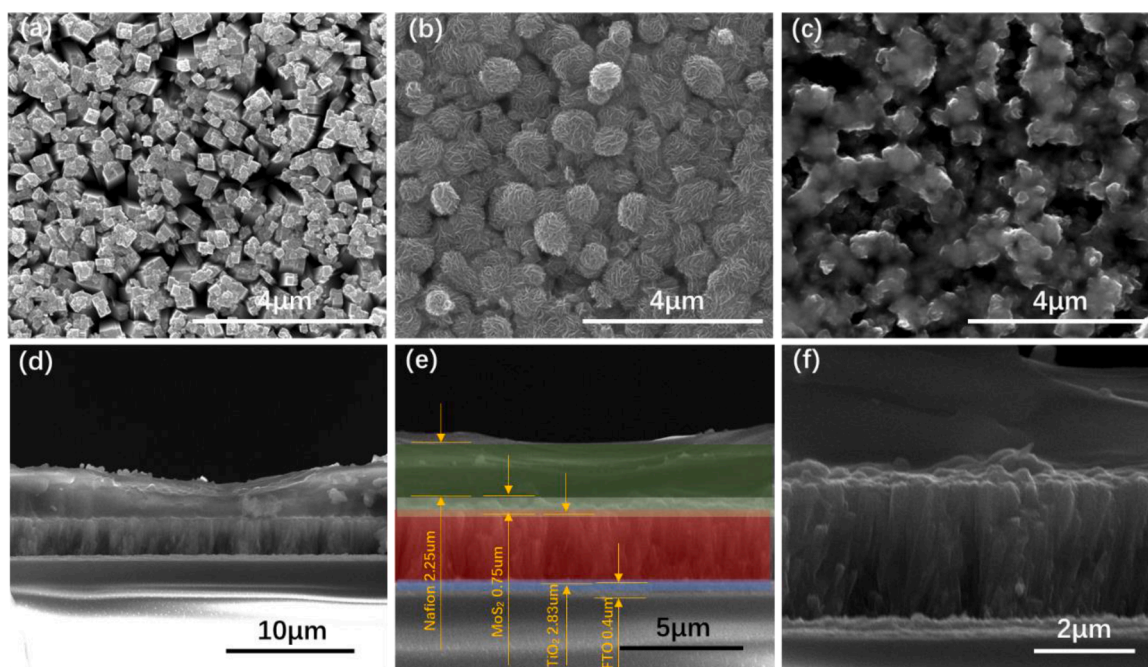
**Fig. 7.** SEM of (a)$TiO_2$, (b)$MoS_2@TiO_2$, and (c)Nafion-protected $MoS_2@TiO_2$ under 30000X under 30 KV, and (d, e, f) cross-section of Nafion-protected $MoS_2@TiO_2$.
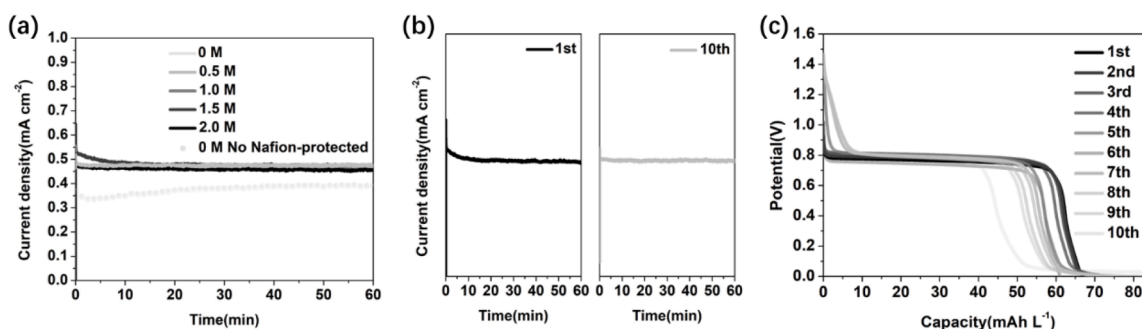


**Fig. 8.** (a) Comparison of bare $MoS_2@TiO_2$ and Nafion-protected $MoS_2@TiO_2$ photoanode in different $NH_4Cl$ concentration, (b)cyclic photocharging with Nafion-protected $MoS_2@TiO_2$ in 1.5 M $NH_4Cl$ and 3.0 M $H_2SO_4$, and (c) discharge experiment in RFB in with 2.5 mL min$^{-1}$ flow rate and light source 100 mW cm$^{-2}$ (AG1.5).

higher photocurrent density values obtained compared to bare $MoS_2@TiO_2$. This is due to the hydrophilic sulfonate groups found in Nafion [58], which enable proton conductivity. After 10 photocharging cycles using an electrolyte containing 1.5 M concentration of $NH_4Cl$ (Fig. 8(b)), the discharge experiments performed after each photo-charging are shown in Fig. 8(c). Energy densities in the range of 42.22–48.63 mW h L$^{-1}$ were obtained after 10 cycles (Table 2). The energy density remains 87.45% after 10 cycles. The state-of-charge

reached 3.54% after 1h-photocharging.

Figs. 9(a) and 9(b) show the EIS results for bare and Nafion-protected $MoS_2@TiO_2$. At a concentration of 1.5 M $NH_4Cl$, the mass transfer rate is highest regardless of the presence of Nafion. However, Nafion-protected $MoS_2@TiO_2$ displays a clearer semi-circle in the Nyquist plot than bare $MoS_2@TiO_2$. This is because Nafion will form a smoother surface, behaving more like a capacitor at the interface electrolyte/photo-electrode. This difference can be modelled in the equivalent circuit as shown in Fig. 9(c) and (d). The equivalent circuit for SRFB can be divided into five parts: photoelectrode, anolyte, membrane, catholyte and carbon electrode, so there will be at least 4 interfaces. The interface of photoelectrode/anolyte can be simplified and represented by R1 and C1/CPE1, while R2 is the resistance of the anolyte, R3 and C2 is the interface anolyte/membrane, R4 is the resistance of the membrane, R5 and C3 is the interface membrane/catholyte, R6 is the resistance of catholyte, and R7 and CPE1 is the interface catholyte/carbon electrode [59,60]. W1 and W2 are used to describe the diffusion of the redox species in the anolyte and catholyte, respectively.

The solar-to-output energy conversion efficiency (SOEE) of the SRFB can be calculated by the following equation:

$$SOEE(\%) = \left( \int I_{dis} \times dt \times \Delta E_0 \right) \Big/ (P_{in} \times S \times t) \times 100 \qquad (7)$$

**Table 2**
Energy density and SOEE in each cycle.

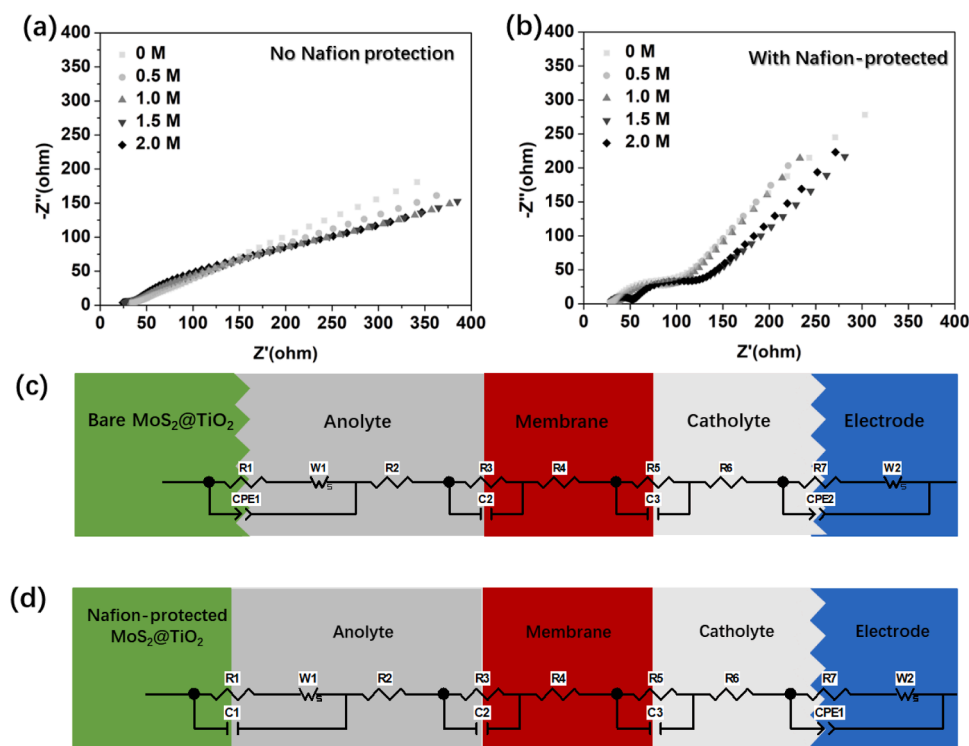| Cycle number | Energy density (mWh L$^{-1}$) | Solar-to-output energy conversion efficiency (SOEE) |
|---|---|---|
| 1 | 48.63 | 9.726% |
| 2 | 48.28 | 9.656% |
| 3 | 48.27 | 9.654% |
| 4 | 47.47 | 9.494% |
| 5 | 46.25 | 9.25% |
| 6 | 45.96 | 9.192% |
| 7 | 45.41 | 9.082% |
| 8 | 43.97 | 8.794% |
| 9 | 43.10 | 8.62% |
| 10 | 42.22 | 8.444% |

**Fig. 9.** EIS of (a) no Nafion-protective and (b) Nafion-protective MoS$_2$@TiO$_2$ in the SRFB, and (c, d) their equivalent circuit.

Where I$_{dis}$ is the discharge current density, $\Delta$E$_0$ is the potential difference, t is the illumination time (1 h), P$_{in}$ is the incident solar power (100 mW cm$^{-2}$), and S is the area of the solar flow cell window (5.0 cm$^2$).

In summary, though the positive effect of NH$_4$Cl in SRFB is not as obvious as in the RFB, here we have introduced an effective photoelectrode-protection method to overcome the photocorrosion of the MoS$_2$@TiO$_2$ photoelectrode during the photocharging in the SRFB [42], thus enhancing the stability and performance of the MoS$_2$@TiO$_2$ electrode. The SOEE of the SRFB can reach 9.726%. This relatively high SOEE benefits from the suitable redox potential of the redox couples and the relative low concentration of the redox species that provide a higher state-of-charge, and therefore exhibits a higher discharge voltage.

## 4. Conclusions

This work shows that the addition of NH$_4$Cl has a positive effect on a redox flow battery and a solar redox flow battery with VOSO$_4$ and AQDS as redox active species. In the cyclic RFB charge-discharge test, the addition of NH$_4$Cl not only enhanced the thermal stability of vanadium ions in the electrolyte, but also improved the charge-discharge capacity of the RFB and significantly improved the voltage and energy efficiencies (17.6% higher). The average discharge capacity loss was the smallest (0.1%) when the NH$_4$Cl concentration was 1.5 M with the discharge capacity of 2.34 Ah L$^{-1}$ just second to the highest one, 2.36 Ah L$^{-1}$. This result are due to the positive effect of the diffusion coefficient of NH$_4$Cl on AQDS and vanadium, which reaches a maximum when the NH$_4$Cl concentration increases to 1.5 M, leading to the best performance. The presence of NH$_4$Cl can not only reduce the energy loss by reducing the resistance of the electrolyte, but also make the ion exchange of the Nafion membrane more efficient, thereby improving the battery performance. However, though NH$_4$Cl can make vanadium ion more dispersive in the electrolyte, the oxygen absorption reaction is also significantly enhanced, which is not conducive to the application in redox batteries that require high charging voltage. In the AQDS electrolyte, AQDS(NH$_4$)$_2$ is produced after charging, with more hydrogen bond in NH$_4^+$ so it will effectively increase charge transfer rate. The

energy density of the SRFB without any bias charging other than solar energy was 48.63 mWh L$^{-1}$, and SOEE efficiency of 9.73%, almost double that of previous work using bare MoS$_2$@TiO$_2$ [42]. The results demonstrated that the Nafion-protected MoS$_2$@TiO$_2$ photoelectrode exhibits good stability in strongly acidic electrolyte compared to the unprotected MoS$_2$@TiO$_2$, successfully confirming the benefits of adding a Nafion layer onto the surface of photoelectrodes, and that can be extended to other semiconductor systems working under light radiation and harsh electrolyte conditions.

## CRediT authorship contribution statement

**Gengyu Tian:** Methodology, Formal analysis, Validation, Data curation, Writing – original draft. **Rhodri Jervis:** Formal analysis, Writing – review & editing. **Ana Jorge Sobrido:** Conceptualization, Methodology, Formal analysis, Writing – review & editing, Supervision, Funding acquisition.

## Declaration of Competing Interest

The authors declare that they have no known competing financial interests or personal relationships that could have appeared to influence the work reported in this paper.

## Acknowledgments

## Supplementary materials

Supplementary material associated with this article can be found, in the online version, at doi:10.1016/j.electacta.2023.142671.

## References

[1] C.S. Lai, G. Locatelli, Economic and financial appraisal of novel large-scale energy storage technologies, Energy 214 (2021), 118954.

[2] E. Sánchez-Díez, E. Ventosa, M. Guarnieri, A. Trovò, C. Flox, R. Marcilla, F. Soavi, P. Mazur, E. Aranzabe, R. Ferret, Redox flow batteries: status and perspective towards sustainable stationary energy storage, J. Power Sources 481 (2021), 228804.

[3] Y. Wen, R. Jervis, New strategies for interrogation of redox flow batteries via Synchrotron radiation, Curr. Opin. Chem. Eng. 37 (2022), 100836.

[4] M.W. Thielke, G. Tian, A.J. Sobrido, Sustainable electrodes for the next generation of redox flow batteries, J. Phys. Mater. 5 (2022), 024004.

[5] J. Vázquez-Galván, C. Flox, C. Jervis, A. Jorge, P. Shearing, J. Morante, High-power nitrided TiO2 carbon felt as the negative electrode for all-vanadium redox flow batteries, Carbon N Y 148 (2019) 91–104.

[6] W. Wang, V. Sprenkle, Redox flow batteries go organic, Nat. Chem. 8 (2016) 204–206.

[7] R. Ye, D. Henkensmeier, S.J. Yoon, Z. Huang, D.K. Kim, Z. Chang, S. Kim, R. Chen, Redox flow batteries for energy storage: a technology review, J. Electrochem. Energy Convers. Storage (2018) 15.

[8] J. Winsberg, T. Hagemann, T. Janoschka, M.D. Hager, U.S. Schubert, Redox-flow batteries: from metals to organic redox-active materials, Angew. Chem. Int. Ed. 56 (2017) 686–711.

[9] W. Lee, B.W. Kwon, Y. Kwon, Effect of carboxylic acid-doped carbon nanotube catalyst on the performance of aqueous organic redox flow battery using the modified alloxazine and ferrocyanide redox couple, ACS Appl. Mater. Interfaces 10 (2018) 36882–36891.

[10] P. Geysens, J. Evers, W. Dehaen, J. Fransaer, K. Binnemans, Enhancing the solubility of 1, 4-diaminoanthraquinones in electrolytes for organic redox flow batteries through molecular modification, RSC Adv. 10 (2020) 39601–39610.

[11] W. Lee, A. Permatasari, Y. Kwon, Neutral pH aqueous redox flow batteries using an anthraquinone-ferrocyanide redox couple, J. Mater. Chem. C 8 (2020) 5727–5731.

[12] M. Park, J. Ryu, W. Wang, J. Cho, Material design and engineering of next-generation flow-battery technologies, Nat. Rev. Mater. 2 (2016) 1–18.

[13] V. Singh, S. Kim, J. Kang, H.R. Byon, Aqueous organic redox flow batteries, Nano Res. 12 (2019) 1988–2001.

[14] B. Huskinson, M.P. Marshak, C. Suh, S. Er, M.R. Gerhardt, C.J. Galvin, X. Chen, A. Aspuru-Guzik, R.G. Gordon, M.J. Aziz, A metal-free organic–inorganic aqueous flow battery, Nature 505 (2014) 195–198.

[15] M. Crossley, The separation of mono-β-, 2, 6-and 2, 7-sulfonic acids of anthraquinone, J. Am. Chem. Soc. 37 (1915) 2178–2181.

[16] M. Gencten, H. Gursu, Y. Sahin, Effect of α-and γ-alumina on the precipitation of positive electrolyte in vanadium redox battery, Int. J. Hydrogen Energy 42 (2017) 25598–25607.

[17] L. Hruska, R. Savinell, Investigation of factors affecting performance of the iron-redox battery, J. Electrochem. Soc. 128 (1981) 18.

[18] S. Hu, L. Wang, X. Yuan, Z. Xiang, M. Huang, P. Luo, Y. Liu, Z. Fu, Z. Liang, Viologen-decorated TEMPO for neutral aqueous organic redox flow batteries, Energy Mater. Adv. 2021 (2021), 9795237.

[19] A.A. Shinkle, A.E. Sleightholme, L.T. Thompson, C.W. Monroe, Electrode kinetics in non-aqueous vanadium acetylacetonate redox flow batteries, J. Appl. Electrochem. 41 (2011) 1191–1199.

[20] W. Lee, G. Park, Y. Kim, D. Chang, Y. Kwon, Nine watt–level aqueous organic redox flow battery stack using anthraquinone and vanadium as redox couple, Chem. Eng. J. 398 (2020), 125610.

[21] M. Mousavi, G. Jiang, J. Zhang, A.G. Kashkooli, H. Dou, C.J. Silva, Z.P. Cano, Y. Niu, A. Yu, Z. Chen, Decoupled low-cost ammonium-based electrolyte design for highly stable zinc–iodine redox flow batteries, Energy Storage Mater. 32 (2020) 465–476.

[22] B. Hu, J. Luo, M. Hu, B. Yuan, T.L. Liu, A pH-neutral, metal-free aqueous organic redox flow battery employing an ammonium anthraquinone anolyte, Angew. Chem. 131 (2019) 16782–16789.

[23] A.K. Manohar, K.M. Kim, E. Plichta, M. Hendrickson, S. Rawlings, S. Narayanan, A high efficiency iron-chloride redox flow battery for large-scale energy storage, J. Electrochem. Soc. 163 (2015) A5118.

[24] A. Khataee, K. Wedege, E. Dražević, A. Bentien, Differential pH as a method for increasing cell potential in organic aqueous flow batteries, J. Mater. Chem. A 5 (2017) 21875–21882.

[25] K. Wedege, E. Dražević, D. Konya, A. Bentien, Organic redox species in aqueous flow batteries: redox potentials, chemical stability and solubility, Sci. Rep. 6 (2016) 1–13.

[26] C. Batchelor-McAuley, Q. Li, S.M. Dapin, R.G. Compton, Voltammetric characterization of DNA intercalators across the full pH range: anthraquinone-2, 6-disulfonate and anthraquinone-2-sulfonate, J. Phys. Chem. B 114 (2010) 4094–4100.

[27] L. Cao, M. Skyllas-Kazacos, D.W. Wang, Solar redox flow batteries: mechanism, design, and measurement, Adv. Sustain. Syst. 2 (2018), 1800031.

[28] W. Li, H.C. Fu, Y. Zhao, J.H. He, S. Jin, 14.1% efficient monolithically integrated solar flow battery, Chem 4 (2018) 2644–2657.

[29] Y. Zhou, S. Zhang, Y. Ding, L. Zhang, C. Zhang, X. Zhang, Y. Zhao, G. Yu, Efficient solar energy harvesting and storage through a robust photocatalyst driving reversible redox reactions, Adv. Mater. 30 (2018), 1802294.

[30] A. Eftekhari, V.J. Babu, S. Ramakrishna, Photoelectrode nanomaterials for photoelectrochemical water splitting, Int. J. Hydrogen Energy 42 (2017) 11078–11109.

[31] Y.L. Lee, C.F. Chi, S.Y. Liau, CdS/CdSe co-sensitized TiO2 photoelectrode for efficient hydrogen generation in a photoelectrochemical cell, Chem. Mater. 22 (2010) 922–927.

[32] W. Yang, R.R. Prabhakar, J. Tan, S.D. Tilley, J. Moon, Strategies for enhancing the photocurrent, photovoltage, and stability of photoelectrodes for photoelectrochemical water splitting, Chem. Soc. Rev. 48 (2019) 4979–5015.

[33] H. Feng, X. Jiao, R. Chen, X. Zhu, Q. Liao, D. Ye, B. Zhang, W. Zhang, A microfluidic all-vanadium photoelectrochemical cell with the N-doped TiO2 photoanode for enhancing the solar energy storage, J. Power Sources 419 (2019) 162–170.

[34] A. Fujishima, K. Honda, Electrochemical photolysis of water at a semiconductor electrode, Nature 238 (1972) 37–38.

[35] L.R. Sheppard, R. Wuhrer, TiO2-Based homojunction photo-electrode for solar-driven water splitting, Int. J. Hydrogen Energy 45 (2020) 9386–9396.

[36] H. Luo, S. Dimitrov, M. Daboczi, J.S. Kim, Q. Guo, Y. Fang, M.A. Stoeckel, P. Samori, O. Fenwick, A.B. Jorge Sobrido, Nitrogen-doped carbon dots/TiO2 nanoparticle composites for photoelectrochemical water oxidation, ACS Appl. Nano Mater. 3 (2020) 3371–3381.

[37] Z. Wei, Y. Shen, D. Liu, F. Liu, An all-vanadium continuous-flow photoelectrochemical cell for extending state-of-charge in solar energy storage, Sci. Rep. 7 (2017) 1–9.

[38] Z. Wei, H. Almakrami, G. Lin, E. Agar, F. Liu, An organic-inorganic hybrid photoelectrochemical storage cell for improved solar energy storage, Electrochim. Acta 263 (2018) 570–575.

[39] W. Zhang, Y. Lin, R. Chen, X. Zhu, D. Ye, Y. Yang, J. Li, Y. Yu, Q. Liao, Self-doped TiO2 nanotube array photoanode for microfluidic all-vanadium photoelectrochemical flow battery, J. Electroanal. Chem. 897 (2021), 115598.

[40] Z. Chen, A.J. Forman, T.F. Jaramillo, Bridging the gap between bulk and nanostructured photoelectrodes: the impact of surface states on the electrocatalytic and photoelectrochemical properties of MoS2, J. Phys. Chem. C 117 (2013) 9713–9722.

[41] W. Teng, Y. Wang, H. Huang, X. Li, Y. Tang, Enhanced photoelectrochemical performance of MoS2 nanobelts-loaded TiO2 nanotube arrays by photo-assisted electrodeposition, Appl. Surf. Sci. 425 (2017) 507–517.

[42] A.B. Jorge, G. Tian, R. Jervis, J. Briscoe, M. Titirici, Efficient harvesting and storage of solar energy of an all-vanadium solar redox flow battery with a MoS2@ TiO2 photoelectrode, J. Mater. Chem. A 10 (2022) 10484–10492.

[43] M.C. Ribadeneyra, L. Grogan, H. Au, P. Schlee, S. Herou, T. Neville, P.L. Cullen, M. D. Kok, O. Hosseinaei, S. Danielsson, Lignin-derived electrospun freestanding carbons as alternative electrodes for redox flow batteries, Carbon N Y 157 (2020) 847–856.

[44] Y. Liu, Y. Li, F. Peng, Y. Lin, S. Yang, S. Zhang, H. Wang, Y. Cao, H. Yu, 2H-and 1T-mixed phase few-layer MoS2 as a superior to Pt co-catalyst coated on TiO2 nanorod arrays for photocatalytic hydrogen evolution, Appl. Catal. B 241 (2019) 236–245.

[45] K. Wedege, J. Azevedo, A. Khataee, A. Bentien, A. Mendes, Direct solar charging of an organic–inorganic, stable, and aqueous alkaline redox flow battery with a hematite photoanode, Angew. Chem. Int. Ed. 55 (2016) 7142–7147.

[46] X. Wu, S. Liu, N. Wang, S. Peng, Z. He, Influence of organic additives on electrochemical properties of the positive electrolyte for all-vanadium redox flow battery, Electrochim. Acta 78 (2012) 475–482.

[47] Y. Yang, Y. Zhang, T. Liu, J. Huang, Improved broad temperature adaptability and energy density of vanadium redox flow battery based on sulfate-chloride mixed acid by optimizing the concentration of electrolyte, J. Power Sources 415 (2019) 62–68.

[48] C. Sun, J. Chen, H. Zhang, X. Han, Q. Luo, Investigations on transfer of water and vanadium ions across Nafion membrane in an operating vanadium redox flow battery, J. Power Sources 195 (2010) 890–897.

[49] B.S. Kilsgaard, S. Haldrup, J. Catalano, A. Bentien, High figure of merit for electrokinetic energy conversion in Nafion membranes, J. Power Sources 247 (2014) 235–242.

[50] Z. Wei, J. Zhao, B. Xiong, Dynamic electro-thermal modeling of all-vanadium redox flow battery with forced cooling strategies, Appl. Energy 135 (2014) 1–10.

[51] M. Gençten, H. Gürsu, Y. Şahin, Electrochemical investigation of the effects of V (V) and sulfuric acid concentrations on positive electrolyte for vanadium redox flow battery, Int. J. Hydrogen Energy 41 (2016) 9868–9875.

[52] A. Tang, J. Bao, M. Skyllas-Kazacos, Studies on pressure losses and flow rate optimization in vanadium redox flow battery, J. Power Sources 248 (2014) 154–162.

[53] K.J. Chae, M. Choi, F.F. Ajayi, W. Park, I.S. Chang, I.S. Kim, Mass transport through a proton exchange membrane (Nafion) in microbial fuel cells, Energy Fuels 22 (2008) 169–176.

[54] M. Rahimnejad, T. Jafary, F. Haghparast, G. Najafpour, A.A. Ghoreyshi, Nafion as a nanoproton conductor in microbial fuel cells, Turk. J. Eng. Environ. Sci. 34 (2011) 289–292.

[55] T.J. Zimudzi, M.A. Hickner, Signal enhanced FTIR analysis of alignment in Nafion thin films at SiO$_2$ and Au interfaces, ACS Macro Lett. 5 (2016) 83–87.

[56] M. Kaur, A. Umar, S.K. Mehta, S. Singh, S.K. Kansal, H. Fouad, O.Y. Alothman, Rapid solar-light driven superior photocatalytic degradation of methylene blue using MoS2-ZnO heterostructure nanorods photocatalyst, Materials 11 (2018) 2254 (Basel).

[57] M. Ludvigsson, J. Lindgren, J. Tegenfeldt, FTIR study of water in cast Nafion films, Electrochim. Acta 45 (2000) 2267–2271.

[58] K.A. Mauritz, R.B. Moore, State of understanding of Nafion, Chem. Rev. 104 (2004) 4535–4586.

[59] T. Wang, J. Lee, X. Wang, K. Wang, C. Bae, S. Kim, Surface-engineered Nafion/CNTs nanocomposite membrane with improved voltage efficiency for vanadium redox flow battery, J. Appl. Polym. Sci. 139 (2022) 51628.

[60] C.N. Sun, F.M. Delnick, D. Aaron, A. Papandrew, M.M. Mench, T.A. Zawodzinski, Probing electrode losses in all-vanadium redox flow batteries with impedance spectroscopy, ECS Electrochem. Lett. 2 (2013) A43.